LETTER

Mapping vibrational surface and bulk modes in a single nanocube

Maureen J. Lagos[1], Andreas Trügler[2], Ulrich Hohenester[2] & Philip E. Batson[1]

Imaging of vibrational excitations in and near nanostructures is essential for developing low-loss infrared nanophotonics[1], controlling heat transport in thermal nanodevices[2,3], inventing new thermoelectric materials[4] and understanding nanoscale energy transport. Spatially resolved electron energy loss spectroscopy has previously been used to image plasmonic behaviour in nanostructures in an electron microscope[5,6], but hitherto it has not been possible to map vibrational modes directly in a single nanostructure, limiting our understanding of phonon coupling with photons[7] and plasmons[8]. Here we present spatial mapping of optical and acoustic, bulk and surface vibrational modes in magnesium oxide nanocubes using an atom-wide electron beam. We find that the energy and the symmetry of the surface polariton phonon modes depend on the size of the nanocubes, and that they are localized to the surfaces of the nanocube. We also observe a limiting of bulk phonon scattering in the presence of surface phonon modes. Most phonon spectroscopies are selectively sensitive to either surface or bulk excitations; therefore, by demonstrating the excitation of both bulk and surface vibrational modes using a single probe, our work represents advances in the detection and visualization of spatially confined surface and bulk phonons in nanostructures.

Vibrational spectroscopy techniques such as infrared absorption, Raman scattering and high-resolution reflection electron energy loss spectroscopy (EELS) enable the study of the vibrational behaviour of extended surfaces and ensembles of nanostructures, using broad beams. For instance, ensembles of heterogeneous magnesium oxide (MgO) nanoparticles have been explored using electrons[9] and photons[10,11], allowing average behaviour over particle orientation and morphology to be obtained; the surface phonon polariton (SPhP) response of micrometre- and submicrometre-scale silicon carbide structures has been studied using photon probes[7,12]; and pump-probe X-ray techniques have been used to image acoustic modes in submicrometre-sized particles[13]. Despite these important advances in experimental design to improve the spatial resolution, the spatial distribution of the several acoustic and optical modes that are present in a single nanoparticle of a few tens of nanometres (<100 nm) still remains to be experimentally determined. Furthermore, unexpected nanoscale surface and shape effects may result in new bulk and surface modes[11,14,15].

Spatially resolved analysis using monochromatic electron beams[16] allows us to identify different types of vibrational modes in nanostructures and to determine their spatial distribution with subnanometre resolution. Atom-wide kiloelectronvolt electron beams are routinely produced and manipulated in scanning transmission electron microscopes (STEM)[17], and such electrons easily transfer energy to the object producing phonon excitations. Theoretical work has described the scattering of swift electrons through phonon excitations in bulk crystals[18–21], but the physical aspects of the spatially resolved inelastic electron scattering from phonons in nanostructures are not well understood. Therefore, experimental EELS vibrational data are needed to test proposed ideas and to validate theoretical models. Here we

measure surface modes and acoustic and optical bulk modes in single MgO nanocubes, and map their spatial distribution as a function of size, using spatially resolved STEM EELS[16], with an energy resolution of 10 meV and a spatial resolution of 1.5–2 Å (Methods).

Figure 1a shows a low-magnification annular dark field (ADF) STEM micrograph of a single MgO nanocube. The cube is suspended by contact with the carbon material through one of its faces, allowing the study of bulk and surface excitations while reducing contributions from nanostructure–substrate coupling effects. A high-resolution ADF
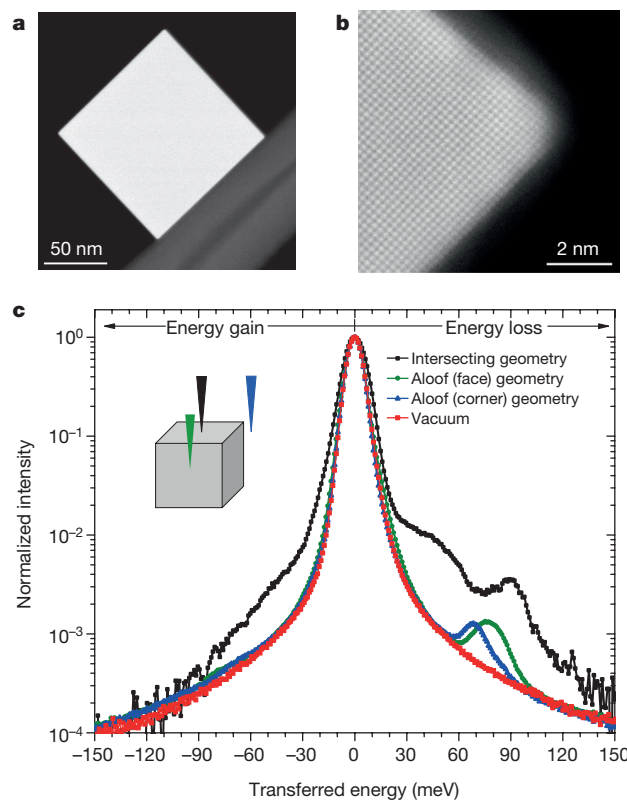

Figure 1 | STEM Imaging and EELS spectra of MgO cubes. a, ADF image of a suspended 150-nm MgO cube. **b,** High-resolution ADF image of a cube oriented along the [001] direction. The cube faces are defined by the (100) atomic planes; the corners and edges are round. A coating layer of about 1–2 nm in thickness is also present. **c,** Typical normalized spectra acquired with the electron beam located in different positions (see inset): green, aloof geometry (beam located near a face); blue, aloof geometry (beam located near a corner); black, intersecting geometry. The spectrum in red is the ZLP spectra acquired in the vacuum. Curves were normalized so that the resonance peak maxima approximate a fractional scattering probability. Regions with positive and negative values of transferred energies are labelled energy loss and energy gain, respectively.

[1]Institute for Advanced Materials, Devices, and Nanotechnology, Department of Materials and Science Engineering, Department of Physics and Astronomy, Rutgers University, Piscataway, New Jersey 08854, USA. [2]Institute of Physics, University of Graz, Universitätsplatz 5, Graz 8010, Austria.

image of the nanocube (Fig. 1b) shows a typical atomic-resolution image. In this [001] projection, each bright spot corresponds to an atomic column that is composed of alternating magnesium and oxygen atoms, with the facets of the cube defined by the (100) atomic planes.

Figure 1c shows typical measured EELS spectra for a MgO nanocube acquired with an electron beam located at different positions (see inset). The spectrum in red shows a typical zero-loss peak (ZLP) profile, acquired in a vacuum region that is very distant from the specimen (approximately 1 μm) to avoid coupling of the fast electron with long-range evanescent phonon fields. The spectra in blue and green were recorded when the beam passed near the cube, but without intersecting it ('aloof' geometry). We find a resonance of approximately 78 meV for a probe travelling next to the cube face (green) and of approximately 69 meV for a probe travelling close to the corner (blue). We also probed the corner and faces of a tilted cube and found the same resonance peaks (Extended Data Fig. 1). Our results for the aloof geometry also show excitation of edge modes of the cube, resulting in an energy-loss peak at around 72 meV (Extended Data Fig. 1c).

These resonances (78 meV, 69 meV and 72 meV) lie in the *reststrahlen* band of the spectrum and are the result of the coupling between the swift electron and SPhP modes of the cube[11], which are composed mainly of surface phonon excitations. Our calculations show that, when the electron passes near the cube, multiple modes (edge, face and corner) can be excited simultaneously with different probabilities (Extended Data Fig. 1). The strength of the excitation is controlled by the interaction between the electron Coulomb field and the polarization charge distribution of the modes, and so it strongly depends on the electron impact parameter.

In Fig. 1c, the spectrum in black was acquired for electrons travelling through the cube. Two bulk excitations are present, an energy-loss peak at around 88 meV and another broad peak with maxima between 40 meV and 50 meV (Fig. 2). The excitation energies are consistent with the energies of phonon modes of bulk MgO (refs 22, 23), and
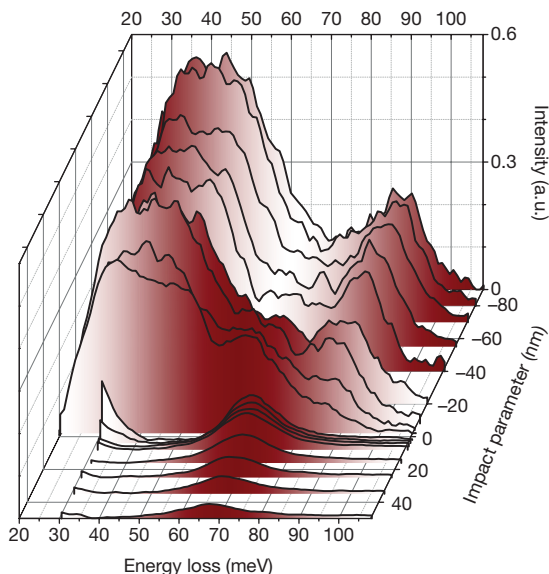
our calculations suggest that the electron can couple with different phonon modes in bulk crystals (Extended Data Fig. 2). The 88-meV peak corresponds to the excitation of the longitudinal optical (LO) mode. The broad 40–50-meV peak results mainly from the coupling with the peak at about 50 meV that corresponds to short-wavelength longitudinal acoustic (LA) modes and transverse optical (TO) modes; contributions from short-wavelength transverse acoustic (TA) modes contribute to the approximately 40-meV excitation. We discuss the bulk scattering in finite-size cubes below.

Bulk and surface modes exhibit energy-gain behaviour on the left side of the ZLP (Fig. 1c). Their inelastic scattering intensities are linked to the loss behaviour through the Boltzmann factor[24], indicating that the phonon scattering in MgO follows the principle of detailed balancing[25]. We also found a ZLP broadening of 3–4 meV when the electron passes through the crystal (black curve in Fig. 1c); we observed this broadening to varying degrees in other material types and thicknesses. A definitive explanation of this broadening requires further investigation.

We now discuss scattering intensities as a function of probe position in suspended cubes of different sizes (45–150 nm), oriented along the [001] direction. We acquired EELS spectra along two high-symmetry lines, starting from a point at the centre of the [001] facet and moving towards the exterior vacuum region, along the [110] and [100] directions. Figure 2 shows background-subtracted EELS spectra recorded along the [110] direction for a 150-nm cube, and illustrates our general findings. Our results for penetrating trajectories show the bulk phonon excitations discussed above. Their bulk scattering intensities are relatively uniform as the probe position is changed, until the probe approaches the surface, at which point the broad 40–50-meV and 88-meV excitation intensities are reduced to about 70% and 10%, respectively, of their bulk values far from the interface. In addition, as the electron probe approaches the surface, the contribution from surface modes to the total scattering increases and is manifested as a small bump at approximately 69 meV in the spectrum.

The bulk scattering near the surface reveals that the LO (88 meV) bulk mode is reduced substantially within distances of about 20 nm from the corner, where intensity is transferred to the surface corner modes. This process is known as the *begrenzung* effect in the context of surface and bulk plasmon behaviour in limited volumes[26] and it seems that a longitudinal *f*-sum-rule-conserving process[25] driving the *begrenzung* effect also operates for phonon modes. Similar behaviour occurs for the approximately 50-meV excitation, although the decrease in intensity is less prominent.

When the electron probe is moved outside the cube, the swift electron predominantly couples to a corner mode (about 69 meV) and the bulk scattering is nearly absent. This finding is in agreement with theory for small ionic particles, which predicts photon absorption for SPhPs, but not for bulk optical modes[10,11]. In addition, the surface scattering decreases the distance from the surface, showing an exponential-like decay for small and moderate impact parameters. For very large impact parameters (>100 nm), the excitation decay rate is slower, probably owing to the long-range dipole nature of the aloof excitation.

The most interesting feature of the EELS results for the [100] direction is the excitation of the face SPhP mode (about 78 meV). Flat surfaces support a Fuchs–Kliewer mode[27], with energy of approximately 80 meV in MgO surfaces[28]. This small difference in excitation energy is mainly attributed to the finite size of the face. As mentioned above, the swift electron also excites the edge and corner modes, but couples more efficiently to the face mode. This results in a surface resonance peak that shifts in energy as the position of the probe is moved along the perimeter of the cube (Extended Data Fig. 1a).

To study the spatial distribution of the vibrational modes we mapped the scattering intensities of the EELS peaks. Figure 3a shows two spatially resolved EELS maps associated with surface modes (about 69 meV and 78 meV) that were acquired in the bulk and aloof positions of a suspended 100-nm MgO cube. Large variations in the
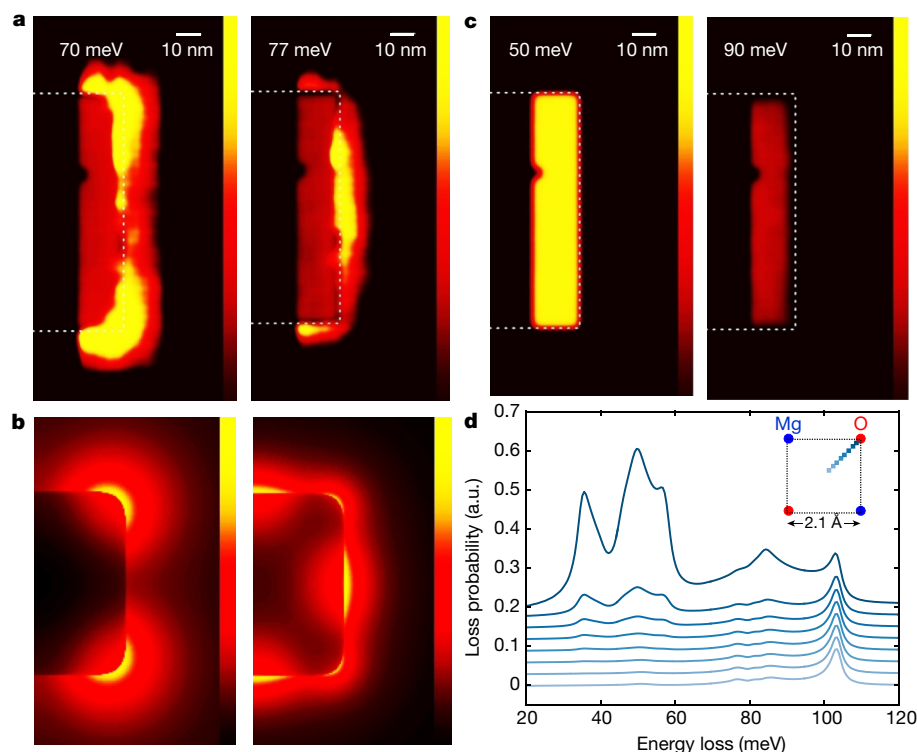

Figure 2 | Spatially dependent EELS scattering acquired along the [110] direction of a 150-nm MgO cube. Two main regions can be defined, one inside and one outside the cube, with negative and positive impact parameter, respectively. The bulk scattering (inside the cube) exhibits two broad main peaks at around 45 meV and 90 meV. The intensity of the broad 40–50-meV excitation is approximately constant in regions away from the interface. The surface scattering (outside the cube) displays only one peak, at approximately 68 meV, which decays as the probe is moved away from the cube. The shading emphasizes the scattering behaviour as a result of the *begrenzung* effect, whereby the surface mode that is excited in the aloof mode (peak at about 68 meV) penetrates partially inside the cube. The 90-meV phonon bulk scattering decreases close to the interface. a.u., arbitrary units.

Figure 3 | Experimental and simulated maps of surface and bulk vibrational EELS scattering on the edge of a single 100-nm MgO cube. **a**, Experimental two-dimensional EELS scattering maps showing the spatial distribution of the corner (left, 70 meV) and face (right, 77 meV) modes. **b**, Simulated EELS maps for the corner (left) and face (right) resonances. **c**, Experimental two-dimensional EELS maps of two bulk phonon excitations (left, 50 meV; right, 90 meV). The bulk modes have been reduced by a factor of about two to emphasize the visualization of the surface modes. The colour scale in **a**–**c** indicates the scattering intensity in arbitrary units. In **a** and **c**, the dotted white box outlines the cube. **d**, Simulated bulk EELS probabilities as a function of the probe position, as it moves from the centre of a square unit cell (lightest blue) to an atom column located at the corner (darkest blue) (see inset).

relative intensity of the polariton modes are evident as the electron probe scanned over the nanocube. The surface phonon patterns are distinctive and show that the vibrational signal is highly localized close to the surfaces. The 69-meV and 78-meV resonances are most intense at the corner and face of the cube, respectively. We estimate the penetration of surface-mode scattering within the cube bulk by subtracting the purely bulk contribution (Methods). We find that the surface modes extend inside the cube a few nanometres (15–20 nm), in agreement with the reported penetration depths for Fuchs–Kliewer modes[28]. Supplementary Video 1 illustrates the spatial distribution of the localized modes.

To obtain insight into the excitation of SPhPs in the nanocube, we performed EELS calculations using a boundary element method[29] that accounts for surface and shape effects and incorporates the long-wavelength surface contributions to the bulk scattering within the dielectric formulation (Methods). Our model captures the main aspects of the dipole scattering physics and produces results that are in good agreement with experiment. Figure 3b shows the simulated EELS probability maps for the localized resonances shown in Fig. 3a. The simulated energies and spatial distribution are in good agreement with the experimental data.

In the aloof geometry, the fast electrons scatter at very small angles (<0.01 mrad), resulting in a small transferred wave vector ($q \approx 0$), which points nearly parallel to the electron trajectory. In this process, the swift electron couples efficiently to the SPhP modes, because their polarization eigenvector has a substantial wavevector component that is parallel to the electron momentum. When the probe intersects the cube near the surface, the excitation of the SPhP modes decrease and the bulk LO modes gradually increase as the swift electron moves into the interior (Fig. 2). In this case, the excitation of the LO mode results from the coupling with parallel and additional transferred perpendicular momentum contributions, in a manner similar to the excitation of longitudinal plasmon oscillations in solids[26].

Figure 3c shows spatially resolved maps for two bulk phonon modes (88 meV and 50 meV). The scattering intensity of the bulk modes are confined inside the cube, decaying quickly close to the cube–vacuum interface, with a more pronounced decay of the LO mode well inside the cube. We found similar results in smaller cubes (100 nm and

45 nm), which demonstrates that bulk phonon modes are also present in smaller nanostructures.

The broad excitations between 40 meV and 50 meV appear to be caused by the large-angle scattered electrons, which carry substantial transverse momentum components ($q_\perp > 0$) and result in excitation of short-wavelength phonon modes. In the limit $q_\perp L \gg 1$ (where L is the cube size), the electron beam is sensitive to suboptical length scales, so that non-dipole scattering processes (impact scattering) can dominate the mapped signal[24]. We use a molecular dynamics approach (Methods) to calculate the EELS scattering due to bulk phonon modes confined in MgO nanocubes with sizes $L < 14$ nm. This method also allows us to include the location of the electron probe within the crystal as a variable, thus revealing scattering variations as the probe is moved. For probe locations approximately equally spaced between atom columns (inset of Fig. 3d), the LO mode dominates the spectrum (curves at the bottom of Fig. 3d), in agreement with our simulations using the long-wavelength dielectric approach. When the probe is displaced towards the atomic columns, acoustic bulk scattering in or near the 40–50-meV range increases substantially, while the LO mode remains approximately the same (curves at the top of Fig. 3d). This finding indicates strong spatially dependent variations in the bulk scattering probability within a unit cell. In our experiments, the probe size was about 1.5–2 Å and its position was not controlled with ångström precision; consequently, an average of the curves in Fig. 3d is expected.

In smaller cubes ($L < 50$ nm) we found that the number of excited surface modes is reduced. Figure 4a shows representative EELS spectra, which were acquired in an external area along the face of a 45-nm cube (see inset) supported on amorphous carbon. The prominent energy-loss peak at approximately 69 meV indicates that the probe couples mainly with corner and edge modes, while a separate face mode is suppressed. We found similar results for suspended cubes of similar size, implying that the face-mode suppression is driven by size effects and not by coupling effects with the amorphous carbon.

Figure 4b shows the experimental EELS maps for the corner- and edge-mode resonance (about 69 meV). The distribution of scattering intensities is uniformly spread around the cube, in contrast to the pattern observed in larger cubes (compare with Fig. 3a). Our EELS probabilities calculations for cubes of different sizes also show that the
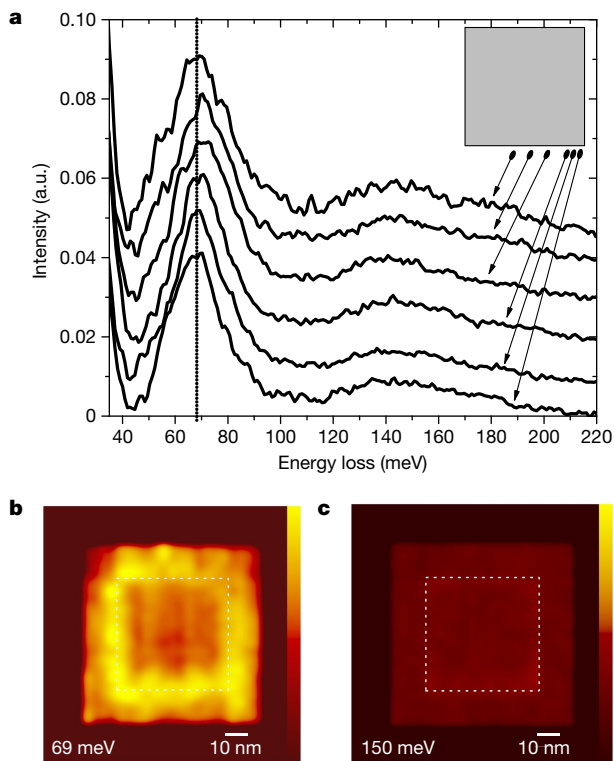
Figure 4 | Size effects on the excitation of surface modes. a, EELS spectra acquired in a region next to the face of a 45-nm cube (see inset) supported in an amorphous carbon substrate. The impact parameter was about 2 nm. All of the EELS resonances peak at approximately 69 meV (dashed line; corner mode). The broad excitation at approximately 150 meV is generated as a result of contributions from excited modes of both the amorphous carbon substrate and the coating layer. **b**, Experimental map of surface phonon scattering (about 69 meV), showing the corner excitations surrounding the cube. **c**, Experimental map of vibrational excitations (about 150 meV) induced by the amorphous carbon substrate. In **b** and **c**, the colour scale indicates the scattering intensity in arbitrary units and the dotted white box outlines the cube.

relative contributions of the corner and edge modes overcome face-mode contributions in smaller cubes (Extended Data Fig. 3). Therefore, our results show that fewer surface excitations can be sustained in smaller nanocubes. Finally, the approximately 150-meV broad excitation (Fig. 4a) probably results from vibrational modes in the amorphous carbon substrate[30] and, possibly, a thin MgO coating layer. Figure 4c shows an EELS map associated with this excitation, wherein the cube intensity disappears into a background that apparently originates in the carbon support.

We have mapped the spatial distribution of surface and bulk phonons in MgO nanocubes, showing both confined bulk and surface phonon modes. This information should be useful for understanding how phonon properties interact with other phonons, plasmons and photons within and outside the nanostructure. We identified a *begrenzung* effect that limits the bulk phonon intensity in the presence of surface behaviour. We found that the size the cube controls the number and energies of surface modes in small cubes. Our results should stimulate investigations towards true atomic-resolution phonon spectroscopy in nanostructures. Our work will be useful for studies of nanoscale energy transport for the development of energy-related processes and technologies.

Online Content Methods, along with any additional Extended Data display items and Source Data, are available in the online version of the paper; references unique to these sections appear only in the online paper.

1. Caldwell, J. D. *et al.* Low-loss, infrared and terahertz nanophotonics using surface phonon polaritons. *Nanophotonics* **4,** 44–68 (2015).
2. Maldovan, M. Sound and heat revolutions in phononics. *Nature* **503,** 209–217 (2013).
3. Venkatasubramanian, R., Siivola, E., Colpitts, T. & O'Quinn, B. Thin-film thermoelectric devices with high room-temperature figures of merit. *Nature* **413,** 597–602 (2001).
4. Snyder, G. J. & Toberer, E. S. Complex thermoelectric materials. *Nat. Mater.* **7,** 105–114 (2008).
5. Nelayah, J. *et al.* Mapping surface plasmons on a single metallic nanoparticle. *Nat. Phys.* **3,** 348–353 (2007).
6. Nicoletti, O. *et al.* Three-dimensional imaging of localized surface plasmon resonances of metal nanoparticles. *Nature* **502,** 80–84 (2013).
7. Hillenbrand, R., Taubner, T. & Keilmann, F. Phonon-enhanced light–matter interaction at the nanometre scale. *Nature* **418,** 159–162 (2002).
8. Caldwell, J. D. *et al.* Atomic-scale photonic hybrids for mid-infrared and terahertz nanophotonics. *Nat. Nanotechnol.* **11,** 9–15 (2016).
9. Geiger, J. Excitation of surface phonons (Fröhlich modes) by keV electrons in small magnesium oxide particles. *J. Phys. Soc. Jpn* **36,** 615 (1974).
10. Genzeland, L. & Martin, T. P. Lattice dynamics of MgO microcrystals. *Phys. Status Solidi (b)* **51,** 101–106 (1972).
11. Fuchs, R. Theory of the optical properties of ionic crystal cubes. *Phys. Rev. B* **11,** 1732–1740 (1975).
12. Caldwell, J. D. *et al.* Low-loss, extreme subdiffraction photon confinement via silicon carbide localized surface phonon polariton resonators. *Nano Lett.* **13,** 3690–3697 (2013).
13. Clark, J. N. *et al.* Ultrafast three-dimensional imaging of lattice dynamics in individual gold nanocrystals. *Science* **341,** 56–59 (2013).
14. Wallis, R. F. Theory of surface modes of vibration in two- and three-dimensional crystal lattices. *Phys. Rev.* **116,** 302–308 (1959).
15. Chalopin, Y. *et al.* Size-dependent infrared properties of MgO nanoparticles with evidence of screening effect. *Appl. Phys. Lett.* **100,** 241904 (2012).
16. Krivanek, O. L. *et al.* Vibrational spectroscopy in the electron microscope. *Nature* **514,** 209–212 (2014).
17. Batson, P. E., Delby, N. & Krivanek, O. L. Sub-ångström resolution using aberration-corrected electron optics. *Nature* **418,** 617–620 (2002).
18. Glauber, R. J. Time-dependent displacement correlations and inelastic scattering by crystals. *Phys. Rev.* **98,** 1692–1698 (1955).
19. Earney, J. J. Phonon scattering of fast electrons by crystals. *Phil. Mag.* **23,** 577–583 (1971).
20. Rez, P. Is localized infrared spectroscopy now possible in the electron microscope? *Microsc. Microanal.* **20,** 671–677 (2014).
21. Forbes, B. D. & Allen, L. Modeling energy-loss spectra due to phonon excitation. *Phys. Rev. B* **94,** 014110 (2016).
22. Peckham, G. The phonon dispersion relation for magnesium oxide. *Proc. Phys. Soc.* **90,** 657–670 (1967).
23. Sangster, M. J. L., Peckham, G. & Saunderson, D. H. Lattice dynamics of magnesium oxide. *J. Phys. C* **3,** 1026–1036 (1970).
24. Ibach, H. & Mills, D. L. *Electron Energy Loss Spectroscopy and Surface Vibrations* 1st edn (Academic Press, 1982).
25. Pines, D. & Nozieres, P. *Theory of Quantum Liquids* 1st edn, Ch. 2 (Academic Press, 1966).
26. Ritchie, R. H. Plasma losses by fast electrons in thin films. *Phys. Rev.* **106,** 874–881 (1957).
27. Fuchs, R. & Kliewer, K. L. Optical modes of vibration in an ionic crystal slab. *Phys. Rev.* **140,** A2076–A2088 (1965).
28. Oshima, C., Aizawa, T., Souda, R. & Ishizawa, Y. Microscopic surface phonons of MgO (100) surface. *Solid State Commun.* **73,** 731–734 (1990).
29. Hohenester, U. & Trügler, A. MNPBEM – a Matlab toolbox for the simulation of plasmonic nanoparticles. *Comput. Phys. Commun.* **183,** 370–381 (2012).
30. Ferrari, A. C. & Robertson, J. Interpretation of Raman spectra of disordered and amorphous carbon. *Phys. Rev. B* **61,** 14095–14107 (2000).

Author Contributions M.J.L. initiated the project and conceived the experiments. M.J.L. prepared the samples and conducted the EELS-STEM experiments. M.J.L. and P.E.B. performed the data analysis and interpretation. U.H. and A.T. developed the theoretical model and performed the theoretical calculations. M.J.L. and P.E.B. wrote the manuscript. All authors read and commented on the manuscript.

Author Information Reprints and permissions information is available at www.nature.com/reprints. The authors declare no competing financial interests. Readers are welcome to comment on the online version of the paper. Publisher's note: Springer Nature remains neutral with regard to jurisdictional claims in published maps and institutional affiliations. Correspondence and requests for materials should be addressed to M.J.L. (maureen.lagos@rutgers.edu).

Reviewer Information *Nature* thanks C. Colliex, P. Rez and the other anonymous reviewer(s) for their contribution to the peer review of this work.

METHODS

Magnesium oxide nanocubes. We produced MgO nanocubes by burning a magnesium wire in air and collected the combustion smoke in a lacey amorphous carbon microscopy grid, obtaining cubes with sizes of 30–500 nm. These cubes are crystalline and their electronic properties have previously been extensively studied using EELS[31]. We chose MgO nanocubes as a case study for three main reasons: (i) MgO is an ionic dielectric with a simple phonon dispersion behaviour, facilitating our ability to understand the aspects of the inelastic electron scattering physics; (ii) MgO nanostructures sustain several SPhPs and bulk phonon modes; and (iii) MgO is readily synthesized as nanocubes over a wide range of sizes, enabling the exploration of size effects on the vibrational response.

Scanning transmission electron microscopy (STEM). The experimental data were obtained using a Nion-UltraSTEM microscope with the Hermes Monochromator operating at 60 kV to improve inelastic scattering cross-sections for vibrational spectroscopy. Four main elements enable the experimental realization of spatially resolved spectroscopic studies of vibrational excitations in nanomaterials: (i) an aberration-corrector enables the formation of an atom-wide electron probe, producing about 1 Å spatial resolution; (ii) a monochromator reduces the energy spread of the field-emitted electrons (250 meV) to about 7.5 meV with 125 ms of acquisition time; (iii) a post-column spectrometer designed for high-dispersion conditions (1 meV per channel) enables a current throughput of about 40% of the incident beam current at optimum resolution; and (iv) a CMOS-based Hamamatsu camera records two-dimensional EELS spectrum images with $2{,}048 \times 500$ pixels.

STEM imaging. The imaging work was done using an electron probe with a convergence semi-angle of 35 mrad. This probe produces about 1-Å resolution with a non-monochromated beam. The transmitted high-angle scattered electrons where collected using a high-angle annular detector with inner and outer collection angles of 80 mrad and 200 mrad, respectively. Electron beam currents for the image acquisitions were 15–25 pA.

EELS data acquisition. The spectroscopy work was performed using conditions of high-beam current probes, which are typically attained using a condenser-lens setting, which favours higher beam current over spatial resolution. We used a probe of 30-mrad convergence semi-angle with a beam current of about 50–75 pA (0.4 μA emission current), producing a probe size of about 1.5 Å with 250-meV-wide energy distribution. Monochromated operation produces a 7.5–10-meV-wide beam (acquisition time 62–1,000 ms) and a beam current of 5–10 pA with emission current stabilities of about 0.05 μA h^{-1}. Under these conditions, the spatial resolution remains between 1.5 Å and 2.0 Å. The EELS spectrometer entrance aperture subtends a 20-mrad (2.5 Å^{-1}) half-angle at 60 kV. With these collection conditions, it should be possible to collect scattering signal from phonon excitations slightly beyond the Brillouin zone boundary for MgO.

EELS spectra were acquired as a function of probe position. For each point of the mapping, 30 EELS spectra were collected and then the beam was blanked for about 15 s and 30 background (dark current) spectra were collected. EELS spectra were acquired in the aloof and intersecting geometries over 500 ms and 1 s, respectively. These values represent the best compromise between improved signal-to-noise ratio and minimized sample drift and beam damage. We also used a beam deflector system installed in the monochromator to blank the electron beam between consecutive data acquisitions to reduce beam damage. Under these conditions, the sample is exposed to the electron irradiation mainly for EELS data acquisition purposes. Once the spectra are acquired we applied a dark image subtraction to each image, aligned multiple exposures using cross-correlation, and finally summed them to produce a single EELS spectrum associated with a single point (Fig. 1c). The collection of multiple EELS data and the generation of a single EELS spectrum were implemented using NION Swift software through Python scripts. ZLP background curves are also acquired in vacuum in a similar manner to that described above.

EELS data processing. The curves shown in Fig. 1c were normalized with respect to the ZLP maximum so that the loss resonance maxima approximate a fractional scattering probability. The inelastic vibrational scattering can reach a few tenths per cent of the ZLP intensity, becoming comparable with typical bulk and surface scattering of plasmon excitations or single-particle excitations. In Fig. 1c, the surface excitation maxima are a few (around three) times smaller than the bulk phonon modes detected in the intersecting geometry. However, an accurate comparison of the magnitudes of bulk and surface spectra cannot be made without analysis of multiple scatterings to higher-energy excitations (including plasmons), which may alter the relative ZLPs and phonon-loss magnitudes.

The curves shown in Fig. 2 were obtained after subtracting a curve that was fitted to the background. We fitted an exponential function $e^{p(x)}$, where $p(x)$ is a third- or fourth-order polynomial for data that was collected in the intersecting or aloof geometries, respectively. The polynomial coefficients are adjusted parameters. The fit is performed over a broad energy window in front of the loss peak. We also

used the tail of the ZLP curve acquired in vacuum to extract the signal collected in the aloof configuration. Our results are consistent with those obtained from the exponential fit. Similar results were obtained when an EELS spectrum is deconvoluted using an experimental ZLP, with the ZLP removal in Fourier space. Finally, a full Fourier logarithmic deconvolution produces consistent results and enables a characterization of the magnitude of the differential scattering cross-section.

Two-dimensional mapping. Mapping of the scattering amplitude was performed using 4-nm steps on a square array. For the maps presented in Figs 3 and 4 we used an array of 35×10 pixels (350 points) and 21×21 pixels (441 points), respectively. This resulted in acquisition of data at about 800 different points. Owing to the short-term stability of the energy resolution in our microscope (typically 5–15 min), all of the experimental data were acquired by hand. This allowed us to have excellent control over the energy resolution (10 meV) as a function of time. Lack of control in the high-energy-resolution conditions can result in broadening of the ZLP, affecting the background-subtraction processing and, consequently, the intensity of the scattering.

Mapped data are rendered for viewing as images using a colour scale (included as a bar on the right in the images). As is evident in Fig. 2, the measured surface polariton scattering intensity is 30%–40% smaller than the bulk scattering intensity and, as per the discussion above, lies partly within the bulk regions and partly outside the cubes, within the vacuum. To render this scattering in a visually informative way, we characterized the bulk scattering in regions of the cube well away from the surfaces and then subtracted this bulk signal everywhere within the cube, revealing intensity variations that we identify as being related to the surface phonon behaviour within the bulk. This process enables us to visualize the penetration of surface-related scattering (Fig. 3a). The measured polaritonic signal in the vacuum closely matches the bulk-related surface signal. The intensities of the rendered bulk and surface signals in the images and associated videos are not displayed using the same colour scale, and so should be viewed as qualitative representations of the energy and spatial variation of the scattered signal. Detailed evaluation of scattering probabilities requires spectral data as shown in Fig. 2.

Vibrational EELS probabilities in an infinite crystal. We calculated the scattering probability using lattice dynamics (rigid-ion approach), including all of the optical and acoustic normal vibration modes of bulk MgO across the Brillouin zone[32,33]. This elementary method has the advantage of analysing the relative contributions of the long- and short-wavelength lattice modes to the inelastic scattering. In particular, we focused on describing the excitation of macroscopic vibrational modes. We write the scattering loss probability for phonon emission at finite temperature in an infinite bulk system as

$$P(\omega, \boldsymbol{q}) \propto \sum_\lambda \int \frac{|F_\lambda(\boldsymbol{q})|^2}{\omega_\lambda(\boldsymbol{q})}(n_q + 1)\delta(\omega - \omega_\lambda(\boldsymbol{q}))\mathrm{d}q_\perp$$

where $q_\perp$ is the transverse component of the transferred momentum $\boldsymbol{q}$, which lies in a plane perpendicular to the electron trajectory, $\omega_\lambda(\boldsymbol{q})$ is the wavevector-dependent mode frequency, n_q is the occupation number, δ is the Dirac delta function, ω is the loss frequency, λ labels the modes, and $F_\lambda(\boldsymbol{q})$ is the coupling strength for fast electron scattering involving the vibrational mode. The coupling factor is given by

$$F_\lambda(\boldsymbol{q}) = \frac{ie}{\pi|\boldsymbol{q}|^2}\sum_k M_k^{-1/2}\mathrm{e}^{-i(\boldsymbol{q}\cdot\boldsymbol{r}_k - q_\perp r_0)}[Z_k\boldsymbol{\xi}_\lambda^*(k, \boldsymbol{q})\cdot\boldsymbol{q}]$$

where Z_k is the effective charge of the kth ion, M_k is its mass, $\boldsymbol{\xi}_\lambda$ are the displacement eigenvectors (polarization of the normal mode of vibration; the asterisk denotes the complex conjugate), $\boldsymbol{r}_k$ are the basis vectors for Mg and O, r_0 is the impact parameter of the electron beam, and e is the elementary charge. For simplicity, the Debye–Waller factor that accounts for the effects of thermal ion motion was not considered. A detailed derivation will be presented elsewhere.

The product of the displacement eigenvector and the effective charge represents an oscillating electric dipole. Therefore, the inelastic electron scattering is controlled by the electric dipole components that produce non-zero values associated with the dot product between the wavevector transfer and the electric dipole term. The dot product of the mode displacement vector and the wavevector transfer ($\boldsymbol{\xi}_\lambda \cdot \boldsymbol{q}$) is the key parameter describing the scattering coupling[18–21]. In the long-wavelength limit ($q \to 0$), the coupling factor reduces to the standard expression that is obtained in the dipole scattering approximation[24].

Vibrational EELS probabilities in finite nanocubes. We performed EELS simulations using the MNPBEM toolbox[29], following the methodology in ref. 34. We studied cubes of different sizes (30–150 nm). For the results in Fig. 3b, we considered a 100-nm cube, discretized by about 5,000 boundary elements, and an experimentally determined dielectric function. In our simulations, we use the fields exerted by the swift electron to compute the surface charges and response fields associated with the induced cube polarization. The electron has to perform work

against these induced fields and, by raster-scanning the electron beam across the nanocube, we obtain a spectral mapping of the electron energy loss. In accordance with the experiments, the kinetic energy of the electrons was set to 60 kV. As described in the main text, we obtain good agreement with experimental data for the scattering in the aloof geometry, in which only surface losses are present, driven by the dipole scattering[24]. In the quasi-static regime, which is applicable in our case and has also previously been assumed[6], the dielectric (plasmonic) response is governed by an energy denominator of the form $\lambda_w + \lambda_k$, where λ_k depends on only the nanoparticle geometry and λ_w on only the material permittivity[11,35]. For this reason, the complete discussion of ref. 6 regarding the plasmon-mode patterns (encoded in λ_k and the corresponding eigenvectors) of a silver nanocube can be applied directly to our MgO cubes, with the only difference being that the different λ_w factor leads to modified peak positions. The shortcoming of this scheme in reproducing the bulk losses can be traced back to our use of a local dielectric function $\varepsilon(\boldsymbol{q} \approx \boldsymbol{0}, \omega)$, which accounts for losses to only the LO phonons. With increasing momentum exchange (impact scattering)[24,36] between the swift electron and the lattice, it becomes possible to additionally excite TO, LA and TA phonon modes with different probabilities (Extended Data Fig. 2). To estimate the importance of such finite-momentum losses, we performed molecular dynamics simulations for MgO cubes of finite sizes (<16 nm). In our approach, we closely follow refs 15 and 37, in which detailed expressions for the short-range interatomic and long-range ionic contributions are provided. We start our simulations by relaxing the ions to their equilibrium positions at zero temperature, and then compute the ensuing time evolution of the ions that are displaced by the swift electron by solving Newton's equations of motion (Verlet algorithm), including a small phonon damping to account for anharmonic phonon decay and other loss channels. The energy loss is obtained using spectral decomposition of the phonon losses. The losses are the same as those suffered by the swift electron that performs work against the Coulomb fields exerted by the phonons. In our simulations, we sum over all ionic pair interactions using a fast multipole expansion for the long-range Coulomb part. Our approach also allows us to vary the position of the electron probe within a unit cell. Similar studies considering changes in the electron probe location within molecular systems are reported in refs 38 and 39. A detailed derivation of our work will be presented elsewhere. Although this method allows us to include a relatively large number of atoms, we were limited in our simulations to cubes with 262,144 atoms, corresponding to cube lengths of 13.5 nm (see also ref. 15 for similar simulations)—about three times smaller than the smallest cube investigated in our experiments. However, as we are primarily interested in bulk losses, which scale linearly with the length of the electron trajectory inside the cube (Fig. 3d), we expect our simplified simulations to provide the correct information, provided that finite-size effects do not play a substantial part in the bulk scattering.

Data availability. Raw data were generated at the State University of New Jersey, Rutgers, and at the University of Graz. Source Data for Figs 1c, 2, 3d and 4a, and Extended Data Figs 1–3 are available in the online version of the paper. Derived data for the map constructions displayed in Figs 3 and 4 are available from the corresponding author upon request.

31. Marks, L. D. Observation of the image force for fast electrons near an MgO surface. *Solid State Commun.* **43,** 727–729 (1982).
32. Senet, P., Lambin, Ph., Vigneron, J. P., Derycke, I. & Lucas, A. A. Phonon surface function of ionic-crystal films: a comparison between microscopic and macroscopic approaches. *Surf. Sci.* **226,** 307–321 (1990).
33. Lambin, Ph., Senet, P. & Lucas, A. A. Validity of the dielectric approximation in describing electron-energy-loss spectra of surface and interface phonons in thin films of ionic crystals. *Phys. Rev. B* **44,** 6416–6428 (1991).
34. García de Abajo, F. J. Optical excitations in electron microscopy. *Rev. Mod. Phys.* **82,** 209–275 (2010).
35. Boudarham, G. & Kociak, M. Modal decompositions of the local electromagnetic density of states and spatially resolved electron energy loss probability in terms of geometric modes. *Phys. Rev. B* **85,** 245447 (2012).
36. Li, C. H., Tong, S. Y. & Mills, D. L. Large-angle inelastic electron scattering from adsorbate vibrations: basic theory. *Phys. Rev. B* **21,** 3057–3073 (1980).
37. Matsui, M. Molecular dynamics study of the structural and thermodynamic properties of MgO crystal with quantum correction. *J. Chem. Phys.* **91,** 489 (1989).
38. Dwyer, C. Localization of high-energy electron scattering from atomic vibrations. *Phys. Rev. B* **89,** 054103 (2014).
39. Saavedra, J. R. M. & Garcia de Abajo, F. J. Phonon excitation by electron beams in nanographenes. *Phys. Rev. B* **92,** 115449 (2015).
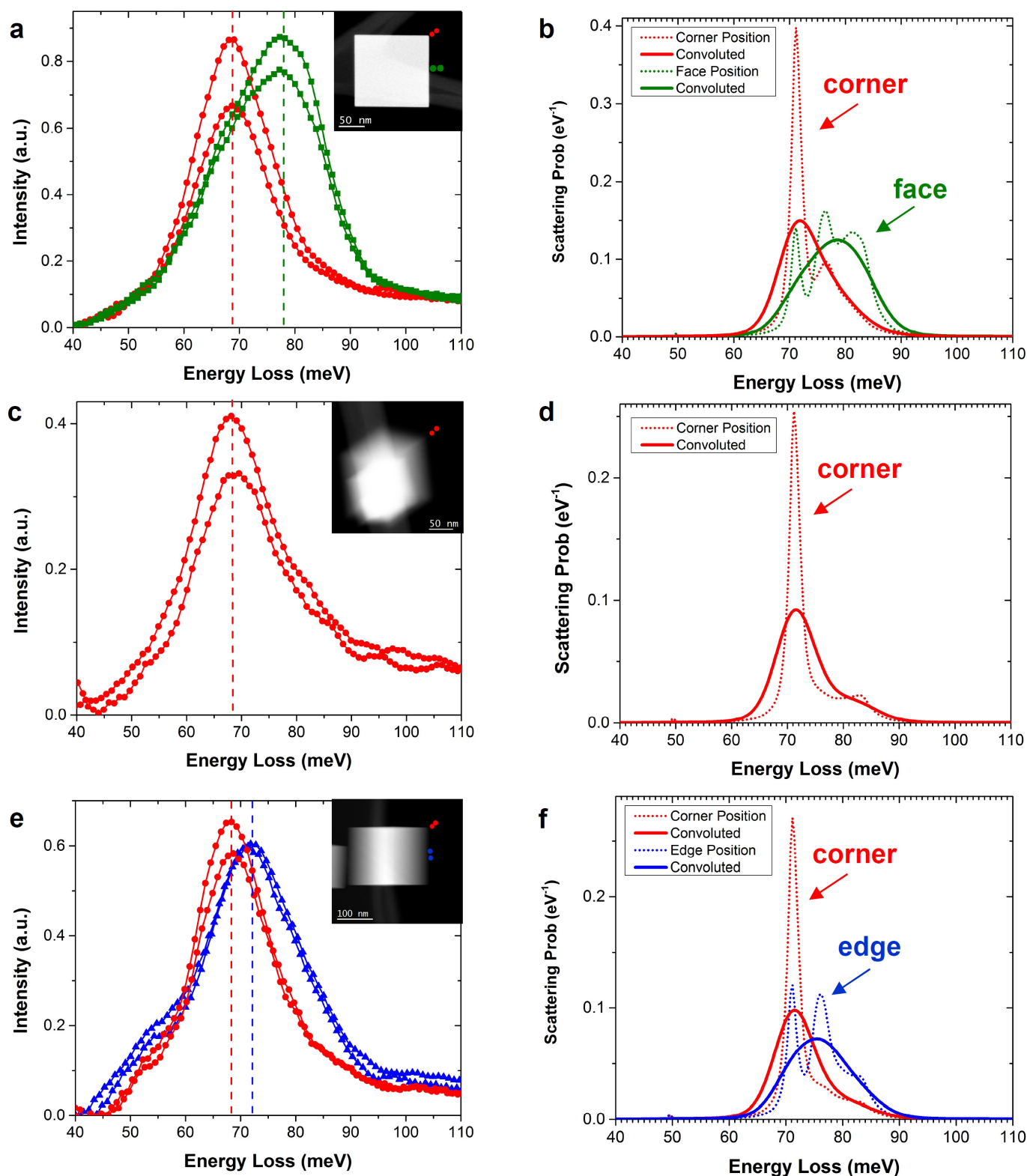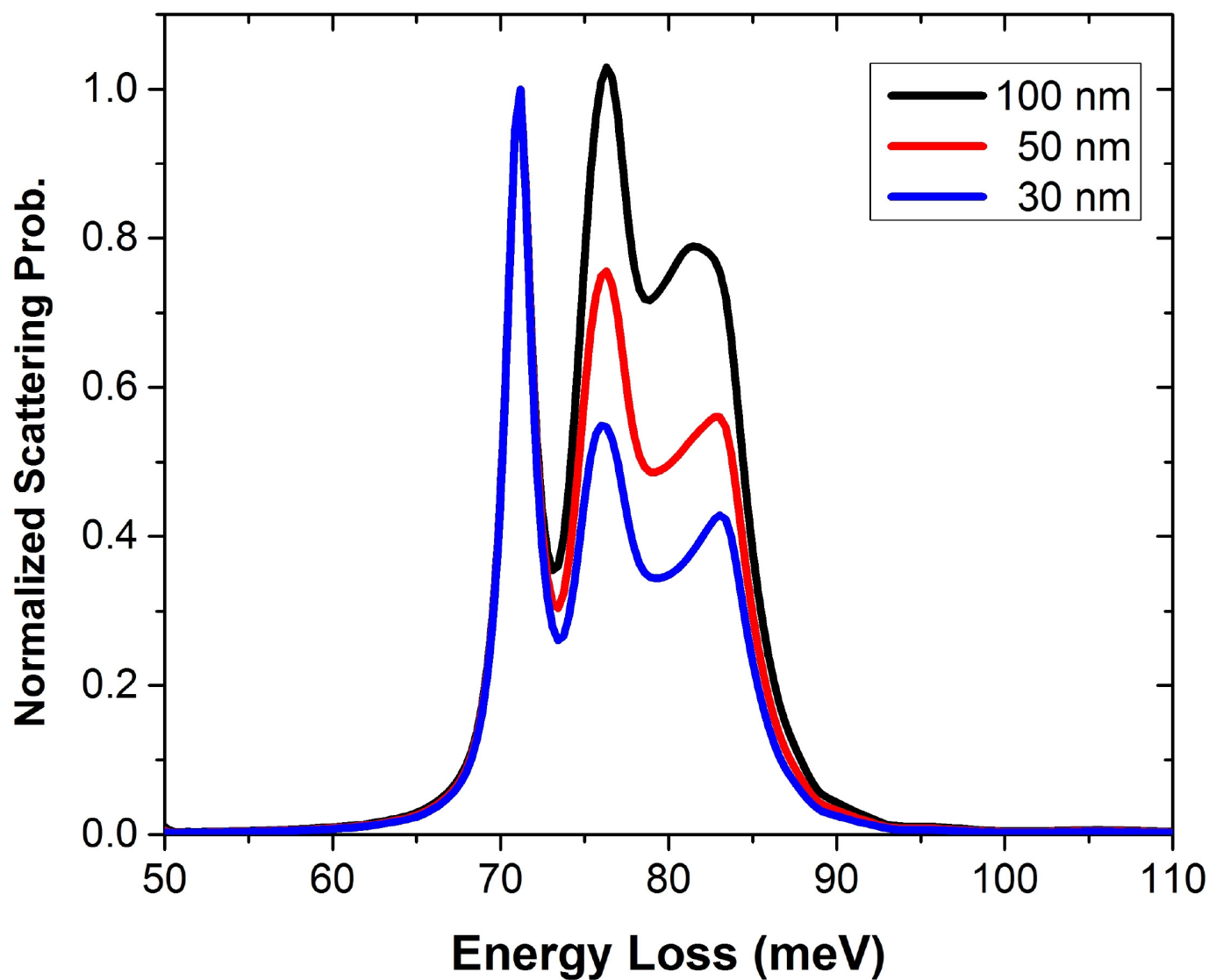
Extended Data Figure 1 | Excitation of corner, face and edge SPhP modes in approximately 150-nm MgO cubes. The excitation occurs in the aloof geometry and the probe positions are indicated by dots in the ADF images (see insets of **a**, **c** and **e**). **a**, **c**, **e**, Experimental EELS spectra for cubes oriented along the [001], [111] and [110] directions, respectively. **b**, **d**, **f**, Simulated EELS probabilities (dotted lines) corresponding to the configurations shown in **a**, **c** and **e**, respectively. The continuous lines are theoretical curves that correspond to the convolution of the dotted lines with a Gaussian function with a width of 10 meV, which accounts for the instrument response. Excitation of the corner mode (red curves) shows up as a peak at approximately 69 meV (vertical dashed red lines in **a**, **c** and **e**). The face-mode excitation (green curves) appears as an asymmetric peak at approximately 78 meV (vertical dashed green line in **a**). This asymmetry is introduced by low-energy contributions of the corner and edge modes. The edge-mode excitation (blue curves) appears as an asymmetric peak at approximately 72 meV (vertical dashed blue line in **e**). Good agreement between the theoretical convoluted curves (**b**, **d**, **f**) and the experimental results (**a**, **c**, **e**) is obtained.
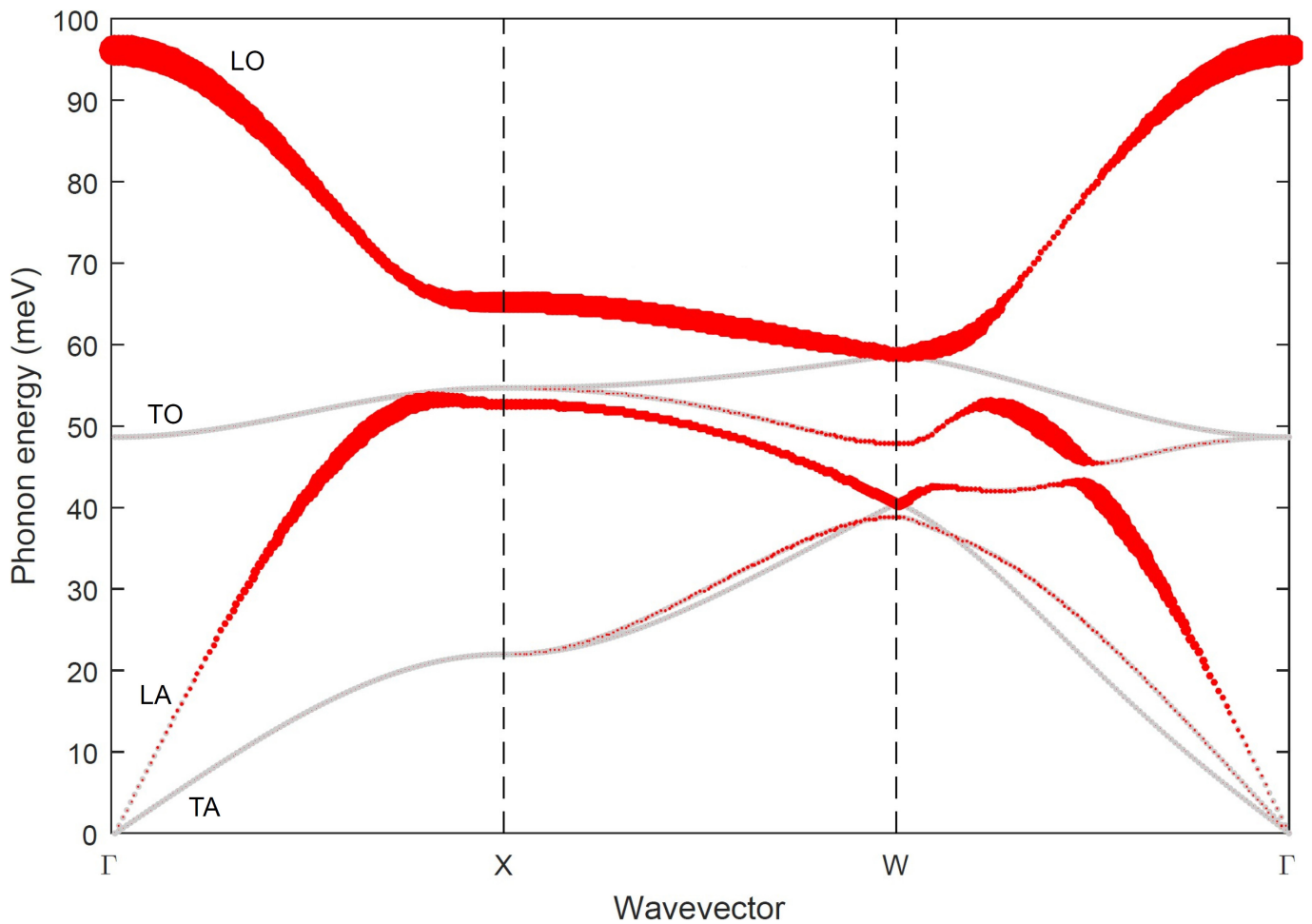
Extended Data Figure 2 | Scattering coupling factor between the swift electron and the phonon modes of a bulk MgO crystal. See Methods. The phonon dispersions (light grey curves) were determined using the rigid-ion approach and most of the calculated phonon frequencies exhibit excellent agreement with the experimental data. The dispersion curves exhibit the typical optical (LO, TO) and acoustic (LA, TA) modes across the first Brillouin zone. The strength of the coupling is represented by the size of the red circles (proportional to $qF_\lambda(\boldsymbol{q})$), which are superposed over the light grey phonon dispersion lines, with larger circles indicating stronger coupling. The swift electron can couple very efficiently to the LO and LA modes, while the transverse modes display weak coupling. An effective coupling can occur with short-wavelength phonons close to the Brillouin zone boundaries through high-angle scattering events.

Extended Data Figure 3 | Simulated EELS probabilities for cubes of different sizes, considering an electron probe in the aloof geometry in the middle of the cube face (5 nm away from the surface). At this location, the probe is able to excite corner, edge and face SPhP modes with different probabilities, as shown in Extended Data Fig. 1b (green curve). The probabilities were normalized with respect to the intensity maximum of the corner resonance (about 71 meV). For the small cubes, the corner mode dominates the excitation spectrum, resulting in small probabilities of face-mode excitations.